INT. J. NUM. METH. HEAT FLUID FLOW, VOL. 4, 47–59 (1994)

AN ASYMPTOTIC SOLUTION FOR THE SINGULARITY AT THE ANGULAR POINT OF THE LID DRIVEN CAVITY

T. STÖRTKUHL*, C. ZENGER AND S. ZIMMER

Institut für Informatik, Technische Universität München, Arcisstrasse 21, D-80290 München. Germany

ABSTRACT

In this paper, we analyse the behaviour of the solution of the Navier–Stokes equations near the corner of the driven cavity where the moving band touches the wall. At this point, the solution is singular. Since the singularity does not depend on the Reynolds number, it is sufficient to study the problem in the case of infinite viscosity, which is governed by the Stokes equations. We present an analytical asymptotic solution near the corner. Furthermore, numerical results are given, which were gained by an efficient multigrid algorithm. We will see that, for decreasing meshsize, the numerical solution converges to the derived analytical solution near the corner.

KEY WORDS Driven cavity Singularities Stokes Multigrid

DERIVATION OF THE ASYMPTOTIC SOLUTION

The plane laminar flow of incompressible fluids is described by the Navier–Stokes equations. In the limit of an infinite viscous fluid these equations are reduced to the Stokes equations which can be written as:

$$\left.\begin{aligned}\Delta\omega &= 0\\ \Delta\psi &= -\omega\end{aligned}\right\} \text{ in } \Omega \tag{1}$$

where ψ denotes the streamfunction and ω the vorticity in the domain Ω. With the velocities u, v in x- and y-direction, respectively, ψ and ω are defined by: $u := \psi_y$, $v := -\psi_x$, $\omega := v_x - u_y$. The system (1) of differential equations can also be written in the form of the biharmonic equation:

$$\Delta\Delta\psi = 0 \quad \text{in } \Omega \tag{2}$$

which is well known in mechanics.

The system (1) is coupled by boundary conditions. Specifying the vector of velocities on the boundary, we get conditions for both ψ and the normal derivative $\partial\psi/\partial n$, but no condition for ω. Now, as a model problem we consider the lid driven cavity that is specified on the unit square

*This work is supported by the Bayerische Forschungsstiftung via FORTWIHR—Bayerischer Forschungsverbund für technisch-wissenschaftliches Hochleistungsrechnen, and by the Deutsche Forschungsgemeinschaft in its Sonderforschungsbereich 342.

0961–5539/94/010047–13$2.00

Received April 1992
Revised September 1993

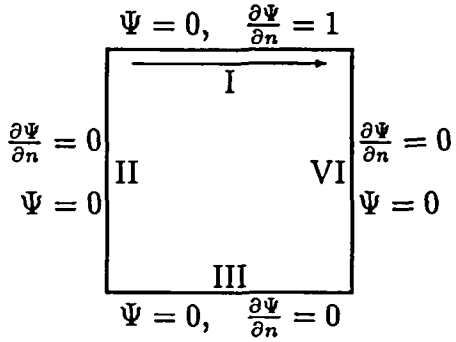

Figure 1 Boundary conditions

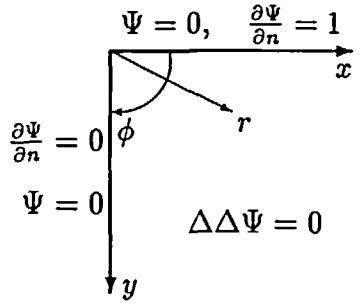

Figure 2 Polar coordinates

$\bar{\Omega} = [0, 1]^2$ by the boundary conditions:

$$\begin{aligned} \psi|_{\mathrm{I,II,III,IV}} &= 0 \\ \left.\frac{\partial\psi}{\partial n}\right|_{\mathrm{II,III,IV}} &= 0 \\ \left.\frac{\partial\psi}{\partial n}\right|_{\mathrm{I}} &= 1 \end{aligned} \tag{3}$$

with boundaries I, II, III, IV as shown in *Figure 1*. As usual $\partial\psi/\partial n$ denotes the normal derivative. We get a laminar flow which is driven on the side *I* with a constant velocity. Thus, we have defined the so-called driven cavity problem. It is well known that this problem possesses singularities in ω at the corner points I × II and I × IV where one side is driven. Now, we will figure out a solution for (1) and the boundary conditions on sides I and II as in *Figure 2*, but neglecting the sides III and IV. Of course, the solution of this weaker problem is not unique. However, any solution will describe a flow at the corner I × II and, assuming that this flow is dominated by local conditions only, our solution must be a good approximation for the initial problem in some suitable region near the corner. Thus, we want to derive an asymptotic analytical solution near the corner point I × II. For this purpose, consider the given problem in terms of polar coordinates as shown in *Figure 2*. Following the argumentation in References 8 and 10 we choose the general trial function:

$$\psi_{(r,\phi)} = R_{(r)} \cdot \chi_{(\phi)} \tag{4}$$

The chosen function (4) yields a separation of the variables r and ϕ where the function $R_{(r)}$ is analytical and $\chi_{(\phi)}$ is some linear combination of transcendent functions. With this in mind, we rewrite the boundary conditions (3) in polar coordinates as:

$$R_{(r)} \cdot \chi_{(0)} = 0 \tag{5}$$

$$R_{(r)} \cdot \chi_{(\pi/2)} = 0 \tag{6}$$

$$\frac{R_{(r)}}{r} \cdot \left.\frac{\partial \chi}{\partial \phi}\right|_{\phi=0} = -1 \tag{7}$$

$$\frac{R_{(r)}}{r} \cdot \left.\frac{\partial \chi}{\partial \phi}\right|_{\phi=\pi/2} = 0 \tag{8}$$

These conditions are inhomogeneous. But condition (7) results in $R_{(r)} \sim r$ which in turn transforms (2) into the following linear ordinary differential equation for χ:

$$\chi^{(4)} + 2 \cdot \chi^{(2)} + \chi = 0 \tag{9}$$

(see References 8 and 1). So, we have chosen the function $\psi_{(r,\phi)} = R_{(r)} \cdot \chi_{(\phi)}$ (see Reference 10) with:

$$\begin{aligned} R_{(r)} &= r \\ \chi_{(\phi)} &= c_1 \cdot \sin(\phi) + c_2 \cdot \phi \cdot \sin(\phi) + c_3 \cdot \cos(\phi) + c_4 \cdot \phi \cdot \cos(\phi) \end{aligned} \tag{10}$$

Thus, we get the following boundary conditions for χ:

$$\begin{aligned} \chi_{(0)} &= 0 \\ \chi_{(\pi/2)} &= 0 \\ \left.\frac{\partial \chi}{\partial \phi}\right|_{\phi=0} &= -1 \\ \left.\frac{\partial \chi}{\partial \phi}\right|_{\phi=\pi/2} &= 0 \end{aligned} \tag{11}$$

and, hence, receive values for the coefficients c_i as follows:

$$c_1 = \frac{-\pi^2}{\pi^2 - 4}, \qquad c_2 = \frac{2 \cdot \pi^2}{\pi^2 - 4}, \qquad c_3 = 0, \qquad c_4 = \frac{4}{\pi^2 - 4} \tag{12}$$

Therefore, we get the solution:

$$\begin{aligned} \psi_{(r,\phi)} &= \frac{r}{\pi^2 - 4} \cdot (-\pi^2 \cdot \sin(\phi) + 2 \cdot \pi \cdot \phi \cdot \sin(\phi) + 4 \cdot \phi \cdot \cos(\phi)) \\ \omega_{(r,\phi)} &= \frac{1}{r} \cdot \frac{1}{\pi^2 - 4} \cdot (4 \cdot \pi \cdot \cos(\phi) - 8 \cdot \sin(\phi)) \end{aligned} \tag{13}$$

In *Figure 3*, we show the levels of the asymptotic solution $\psi_{(r,\phi)}$ of (13) near the corner I × II, which can be identified as the streamlines of the flow. The left upper corner in *Figure 3* corresponds to the corner point I × II in *Figure 1*.

THE ALGORITHM

The given problem can be solved by discretizing the biharmonic equation (see References 2 and 6) or by using the system of equations (1) (see References 9 and 4). In system (1), we obtain two Poisson equations that can be solved efficiently by standard multigrid methods (see Reference

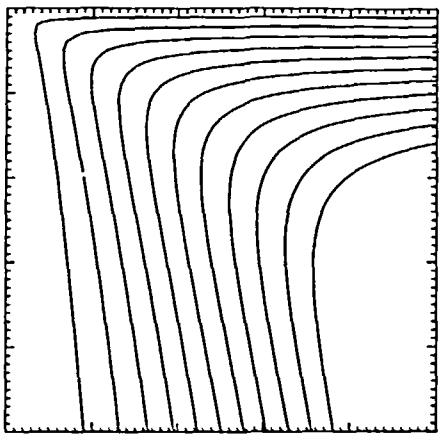

Figure 3 Levels of the asymptotic solution $\psi_{(r,\phi)}$, left upper corner

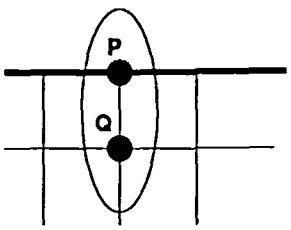

Figure 4 Side I, equations in P and Q are solved simultaneously

5). The crucial point is the coupling of these equations by the boundary conditions. So, we have to compute ω-values on the boundaries, and this has to be done very carefully. Our method is very close to that of Reference 9. But we discretize the system (1) by a finite-element-method using bilinear pagoda functions. Thus, on an equidistant grid $\bar{\Omega}_{n,n}$ on the unit square $\bar{\Omega} = [0, 1] \times [0, 1]$ with meshsize $h = 2^{-n}$ in x- and y-direction, we get the following discrete problem for the inner points of $\bar{\Omega}_{n,n}$:

$$\begin{aligned} L_h \cdot \omega^h &= f_\omega^h \\ L_h \cdot \psi^h + I_h \cdot \omega^h &= f_\psi^h \end{aligned} \tag{14}$$

L_h denotes the standard 9-point finite-element-stencil of the Laplacian operator and I_h the corresponding stencil for the identity operator. On the finest grid, we have $f_\omega^h = f_\psi^h = 0$. On the coarser grids, f_ω^h and f_ψ^h denote the restricted residuals with respect to ω^h and ψ^h.

To compute the values for ω on the boundaries, we discretize the equation $\Delta\psi = -\omega$ on the boundary. On the northern boundary I (see *Figures 1, 2* and *4*), for example in point P, this yields the equation:

$$\frac{1}{3h^2}\begin{bmatrix} \bullet & \bullet & \bullet \\ \frac{1}{2} & -4 & \frac{1}{2} \\ 1 & 1 & 1 \end{bmatrix}\psi^h + \frac{1}{9}\begin{bmatrix} \bullet & \bullet & \bullet \\ \frac{1}{2} & 2 & \frac{1}{2} \\ \frac{1}{4} & 1 & \frac{1}{4} \end{bmatrix}\omega^h = -\frac{1}{h} \tag{15}$$

where the term $-(1/h)$ on the right hand side emerges from the Neumann boundary condition $\psi_n = 1$ on the boundary I. On the other boundaries, this term equals zero. Analogously, we

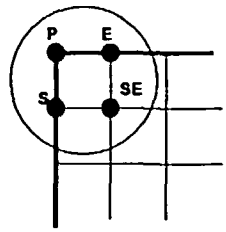

Figure 5 Corner I × II, equations for all four named points are solved simultaneously

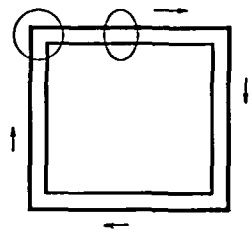

Figure 6 Computation of the boundary values

obtain for each corner point (see *Figure 5*) the equation:

$$\frac{1}{3h^2}\begin{bmatrix} \bullet & \bullet & \bullet \\ \bullet & -2 & \frac{1}{2} \\ \bullet & \frac{1}{2} & 1 \end{bmatrix}\psi^h + \frac{1}{9}\begin{bmatrix} \bullet & \bullet & \bullet \\ \bullet & 1 & \frac{1}{2} \\ \bullet & \frac{1}{2} & \frac{1}{4} \end{bmatrix}\omega^h = -\frac{1}{2h} \tag{16}$$

where the factor $-(1/2h)$ arises from the Neumann condition on side I of the cavity.

The equations (15) and (16) hold on the finest grid. On the coarser ones, the right hand sides equal the restricted residuals on the boundaries. The equations (15) and (16) must be solved for ω in the point P. Note that all values of ψ on the boundaries are zero.

Furthermore, in an iterative process, we get rather large changes of the boundary values of ω due to the fact that the values of ψ are weighted by the factor $1/3h^2$ in (15) and (16). Therefore, slight changes on inner points have large effects on the boundary values. To avoid oscillations and divergence of our multigrid algorithm, we perform one relaxation step for boundary points and the neighbouring inner points simultaneously. Thus, we solve (15) in P and the system of equations (14) in Q (see *Figure 4*) simultaneously. In the case of a corner, the corresponding equations in P, E, S and SE (see *Figure 5*) are solved simultaneously. Thus, not only the values on the boundary but also the values of the neighbouring inner points are computed in Gauss–Seidel fashion as shown in *Figure 6*.

With bilinear interpolation and the weighted restriction as the transfer operators between the grids, we use the Galerkin approximation and get the same discrete operator on every grid. We use the usual multigrid method with ν_1 pre- and ν_2 post-smoothing steps over the boundary as explained above and over the remaining inner points. We can employ the V-cycle or the W-cycle of the multigrid method. The scheme of the multigrid cycle is shown in *Table 1*. The superscript b denotes the modified operators on the boundary and $H = 2 \cdot h$ the meshsize of the coarser grid.

To prove the quality of our algorithm, and for reasons of comparison, we have implemented and solved the model problem given in Reference 9.

Table 1 (ν_1, ν_2, γ)MG-cycle

if $h = \frac{1}{2}$

Solve the corresponding system of linear equations for the 8 boundary points and the one inner point simultaneously

else

1. Relax ν_1 times
   (a) on the boundary and the neighbouring inner points
   $$L_h^b \psi_h + I_h^b \omega_h = f_\omega^h$$
   (b) on the inner points
   $$L_h \omega_h = f_\omega^h$$
   $$L_h \psi_h + I_h \omega_h = f_\psi^h$$
2. Compute the residuals
   $$\text{res}_\omega^h = f_\omega^h - L_h^b \psi_h - I_h^b \omega_h$$
   $$\text{res}_\omega^h = f_\omega^h - L_h \omega_h$$
   $$\text{res}_\psi^h = f_\psi^h - L_h \psi_h - I_h \omega^h$$
3. Perform the restriction
   $$f_\omega^H = R_h^{b,H} \text{res}_\omega^h$$
   $$f_\omega^H = R_h^H \text{res}_\omega^h$$
   $$f_\psi^H = R_h^H \text{res}_\psi^h$$
4. $\omega^H = 0.0$, $\psi^H = 0.0$
5. Apply the (ν_1, ν_2, γ)MG-cycle γ times on
   $$L_H^b + I_H^b \omega_H = f_\omega^H$$
   $$L_H \omega_H = f_\omega^H$$
   $$L_H \psi_H + I_H \omega_H = f_\psi^H$$
6. Correction of the values on the fine grid
   $$\omega_h = \omega_h + P_H^h \omega^H$$
   $$\psi^h = \psi^h + P_H^h \psi_H$$
7. Relax ν_2 times
   $$L_h^b \psi_h + I_h^b \omega_h = f_\omega^h$$
   $$L_h \omega_h = f_\omega^h$$
   $$L_h \psi_h + I_h \omega_h = f_\psi^h$$

NUMERICAL RESULTS

First, we consider the asymptotic convergence of our algorithm. In *Table 2*, the measured dominant factor in the expansion of the error of the numerical solution is shown. It is given by (see Reference 9):

$$R_\psi = \log_{H/h}\left(\frac{|\psi_H - \psi_{H/2}|_2}{|\psi_h - \psi_{h/2}|_2}\right), \qquad R_\omega = \log_{H/h}\left(\frac{|\omega_H - \omega_{H/2}|_2}{|\omega_h - \omega_{h/2}|_2}\right) \tag{17}$$

The norm is the global discrete L_2-norm. Thus, we see that the global discretization error is of the order $O(h^2)$. In the same way as in Reference 9, we have also measured the convergence factors by Mises vector iterations. The results are shown in *Tables 3* and *4* for the V- and W-cycle, respectively. We see that for the V-cycle the convergence factors are dependent on the meshsize h. Only for the combinations of $\nu_1 = 2, \nu_2 = 1$ and $\nu_1 = 2, \nu_2 = 2$, the V-cycle converges

Table 2 Asymptotic convergence of the discrete solution

H	h	R_ψ	R_ω
$\frac{1}{2}$	$\frac{1}{4}$	2.28	2.04
$\frac{1}{4}$	$\frac{1}{8}$	2.12	2.05
$\frac{1}{8}$	$\frac{1}{16}$	2.05	2.03
$\frac{1}{16}$	$\frac{1}{32}$	2.02	2.02
$\frac{1}{32}$	$\frac{1}{64}$	2.01	2.01
$\frac{1}{64}$	$\frac{1}{128}$	2.01	2.00
$\frac{1}{128}$	$\frac{1}{256}$	2.00	2.00

Table 3 V-cycle

(ν_1, ν_2)	(1, 0)	(2, 0)	(3, 0)	(1, 1)	(2, 1)	(2, 2)
$\frac{1}{8}$	1.65	0.13	0.07	0.14	0.08	0.04
$\frac{1}{16}$	2.14	0.22	0.13	0.27	0.09	0.05
$\frac{1}{32}$	13.9	0.53	0.14	0.41	0.20	0.08
$\frac{1}{64}$	—	1.14	0.24	0.55	0.27	0.12
$\frac{1}{128}$	—	—	0.51	0.70	0.36	0.16
$\frac{1}{256}$	—	—	1.00	0.85	0.44	0.20
$\frac{1}{512}$	—	—	—	0.98	0.52	0.20

Table 4 W-cycle

(ν_1, ν_2)	(1, 0)	(2, 0)	(3, 0)	(1, 1)	(2, 1)	(2, 2)
$\frac{1}{8}$	0.28	0.13	0.06	0.14	0.06	0.03
$\frac{1}{16}$	0.34	0.18	0.08	0.16	0.07	0.04
$\frac{1}{32}$	0.35	0.19	0.07	0.17	0.07	0.05
$\frac{1}{64}$	0.36	0.21	0.07	0.18	0.07	0.05
$\frac{1}{128}$	0.44	0.22	0 07	0.19	0.07	0.05
$\frac{1}{256}$	0.53	0.22	0.07	0.19	0.07	0.05
$\frac{1}{512}$	0.57	0.23	0.08	0.19	0.07	0.06

on all grids. In the case of the W-cycle, the convergence factors are dependent on the meshsize only for the two combinations $\nu_1 = 1, \nu_2 = 0$ and $\nu_1 = 2$, $\nu_2 = 0$. Therefore, these results are comparable to those of Reference 9.

NUMERICAL EXPERIMENTS

In this section, we present the results of our numerical experiments obtained by the multigrid algorithm that was explained in the previous section. We want to show the correctness of the analytical solution by comparison with the best numerical solution which is assumed to be a very good approximation to the unknown exact solution.

Let us have a look at ω. First, in *Figure 7* we see that the computed ω^h grows to very high values at the corners I × II and I × IV. However, the values of ω^h in the rest of the domain are small. *Table 5* lists the values in the corner point with the meshsize $h = 2^{-n}$ of the used grid

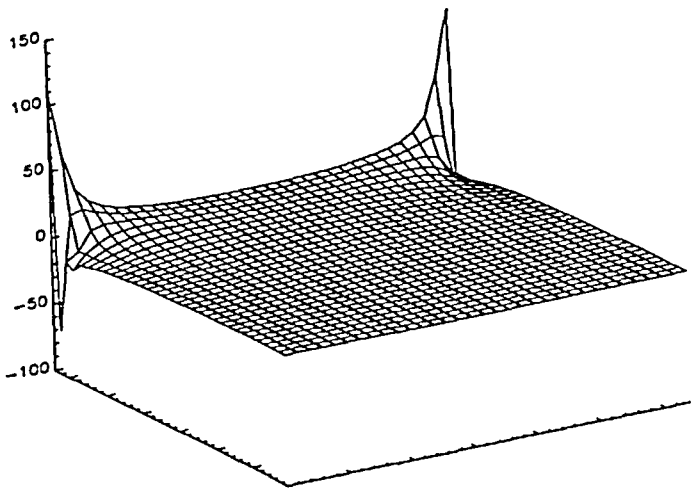

Figure 7 Computed solution ω^h, $h = 2^{-5}$

Table 5 Values of ω at the corner, grid $\Omega_{n,n}$ with meshsize 2^{-n}

n	2	3	4	5	6	7	8	9
ω	13.86	27.71	55.43	110.9	221.7	443.4	886.8	1774

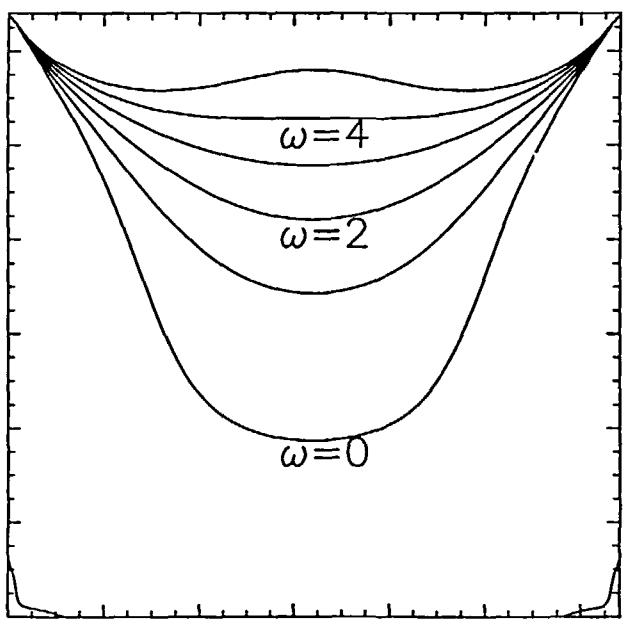

Figure 8 Levels of ω^h, $h = 2^{-7}$

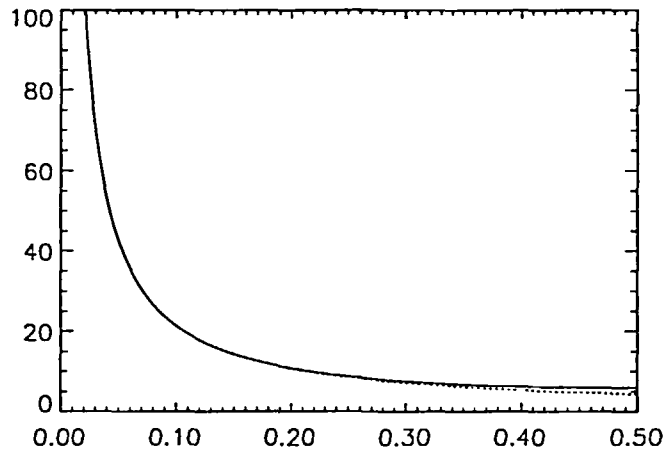

Figure 9 Asymptotic $\omega(\cdots)$ and computed ω^h on side I with meshsize $h = 2^{-9}$

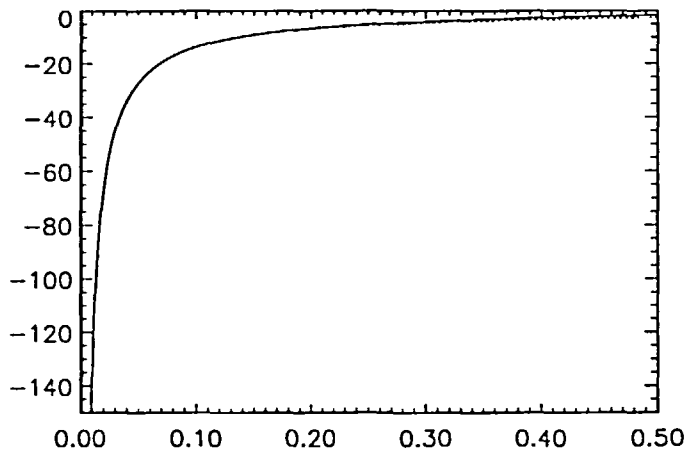

Figure 10 Asymptotic $\omega(\cdots)$ and computed ω^h on side II with meshsize $h = 2^{-9}$

$\Omega_{\pi,\pi}$. With halving the meshsize h, the value of ω^h in the corner point doubles. This means that ω^h is proportional to $1/h$, i.e. $\omega \sim 1/r$. Furthermore, let us study *Figure 9*. There, the computed ω^h together with the asymptotic solution ω from (13) along the driven side I are shown. We see that the numerical solution and the asymptotic one coincide in some region near the corner point I × II. *Figure 10* shows both the computed ω^h and the asymptotic solution ω from (13) on the wall (side II in *Figure 1*). Here, the numerical solution also converges to the asymptotic one apart from some oscillatory behaviour (see *Figure 10*) which is due to the pollution effect of the singularity (see for example Reference 1).

Second, in our asymptotic solution (13) ω becomes zero for $\tan(\phi_0) = \pi/2$, i.e., $\phi_0 = 57.52°$. In *Figure 8*, we see some levels of the computed solution ω^h, especially the level with $\omega^h = 0.0$ which encloses an angle ϕ with the driven side I (see also *Figure 1*). In *Table 6*, we have listed some measured angles of the computed solution on the grid $\Omega_{8,8}$. The angles are taken at points of lines which are at distance d (in *Table 6* measured in multiples of the meshsize $h = 2^{-8}$) from the driven side I and where ω^h changes its sign. For small values of d, again we can see the

Table 6 Angles, enclosed by the null level and the driven side I

d/h	1	2	3	4	5	6	7	8	9	10	11	12	13	14	15
$\phi[^\circ]$	63.4	53.1	63.4	58.0	55.0	59.7	57.3	55.5	58.6	57.0	55.7	58.0	56.8	58.7	57.7

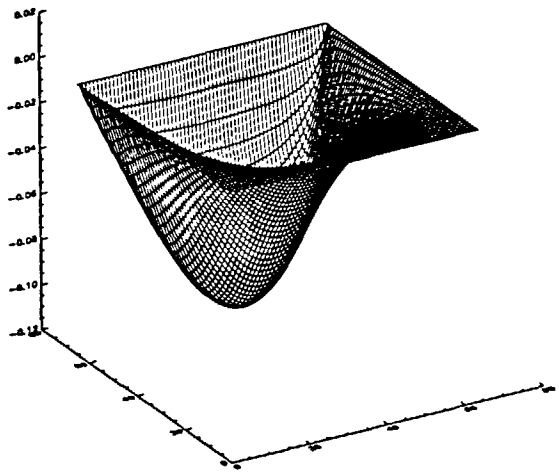

Figure 11 Computed solution ψ^h

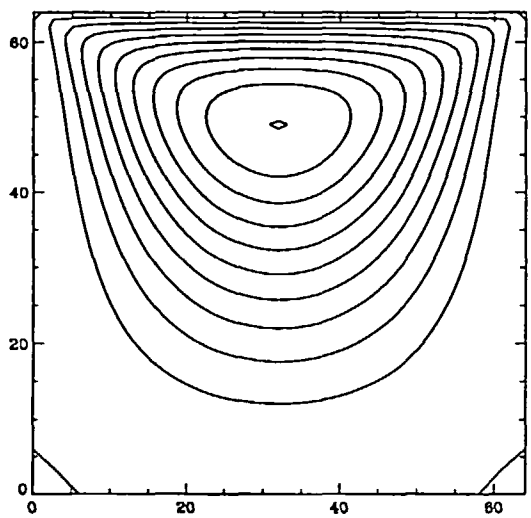

Figure 12 Levels of ψ^h

pollution effect of the singularity at the corner, because the values of ϕ near the corner oscillate about ϕ_0. But all other values are in quite a good accordance to ϕ_0 of the asymptotic solution. Therefore, the coefficients of (13) are the correct ones. Now, we have a look at ψ. The computed solution ψ^h is shown in *Figure 11*, and in *Figure 12* we show its levels. The asymptotic solution ψ of (13) in *Figure 3* and the computed solution ψ^h of *Figure 12* naturally allow only qualitative

comparisons. We see that *Figure 3* is the left upper sector of *Figure 12*. Again, the asymptotic solution is equivalent to the numerical one.

CONCLUSIONS

In the previous section, we have shown that our mathematical model is confirmed by our numerical experiments. But does the asymptotic solution (13) describe the physical reality? To answer this question, we want to make an estimation of the force F which is necessary to drive the fluid in the cavity by using the solution (13). Since we look at the laminar flow of a Newton fluid, Newton's law holds and provides for the shear stress $\tau = F/dx = \eta \cdot \partial u/\partial y$, where u denotes the velocity in x-direction, η denotes the viscosity of the fluid (coordinate system like in *Figure 2*), and dx is some element of length in our two-dimensional case. We look at τ on side I. Then, $\partial u/\partial y$ can be expressed by:

$$\omega|_{r,\phi=0} = \left(\frac{\partial u}{\partial y} - \frac{\partial v}{\partial x}\right)\bigg|_{r,\phi=0} = \frac{\partial u}{\partial y}\bigg|_{r,\phi=0} = \frac{\partial u}{\partial y}\bigg|_{x,\phi=0} \tag{18}$$

because the velocity in y-direction is $v = 0$ on side I. Therefore, the whole force F for an interval $[0, L]$, where the asymptotic solution (13) is valid, is given by:

$$F = \int_0^L \tau \, dx \approx \eta \int_0^L \left(\frac{\partial u}{\partial y}\right) dx = \eta \int_0^L \omega|_{r,\phi=0} \, dr = \eta \cdot \frac{4.0 \cdot \pi}{\pi^2 - 4.0} \cdot \int_0^L \frac{1}{r} \, dr \tag{19}$$

We see that the integral does not exist: F becomes an infinite force. This means that the driven cavity is not a realistic physical problem. To prevent the force F from growing to infinity we have to integrate only up to a distance d of the corner point I × II and get

$$F_d = \eta \cdot \int_d^L \omega|_{r,\phi=0} \, dr = \eta \cdot \frac{4.0 \cdot \pi}{\pi^2 - 4.0} \cdot (\ln(L) - \ln(d)) \tag{20}$$

In this way, we modify our mathematical model, because we allow that the boundary conditions (3) are no longer valid in a region of size d around the corner point I × II. Hence, our derived solution (13) is also not valid in this region. We have to allow a small slot between the driven band and the wall so that a little fluid can flow into the cavity. We assume that this occurs only in a small region of size of d around the corner and that the solution is not disturbed farther away. Then, a good approximation of the whole force to drive the lid is given by

$$F_{\text{lid}} = 2 \cdot F_d + \eta \cdot \int_L^{1-L} \omega^h \, dr \tag{21}$$

where the second term is independent of d, and F_d grows logarithmically with d^{-1}. Thus we expect that the force to drive the band should increase logarithmically with decreasing distance between the moving band and the wall in a physical experiment. The numerical results are shown in *Table 7* where the integral $f_{\text{int}} = \int_h^{1/4} \omega^h dr$ alongside I was computed. By comparison with the analytical integral F_d of (20), the numerical proportionality constant C can be evaluated and is about the analytical value $C = 4.0 \cdot \pi/(\pi^2 - 4.0) = 2.141$.

Table 7 Values of the integral taken at side I for various grids with meshsize h and with $L = \frac{1}{4}$

h	$\frac{1}{32}$	$\frac{1}{64}$	$\frac{1}{128}$	$\frac{1}{256}$	$\frac{1}{512}$
f_{int}	4.665	6.020	7.437	8.890	10.35
C	2.243	2.171	2.145	2.136	2.134

Table 8 Angles, enclosed by the null level and the driven side I for a laminar flow with Re = 20

$d \times 10^{-3}$	2.61	3.75	4.95	6.21	7.54	8.94	10.4	12.0	13.6	15.3	17.1	19.1	21.1	23.2
ϕ[°]	68.8	61.1	67.3	62.9	60.0	58.0	56.6	55.5	58.8	57.7	56.9	56.1	55.5	55.0

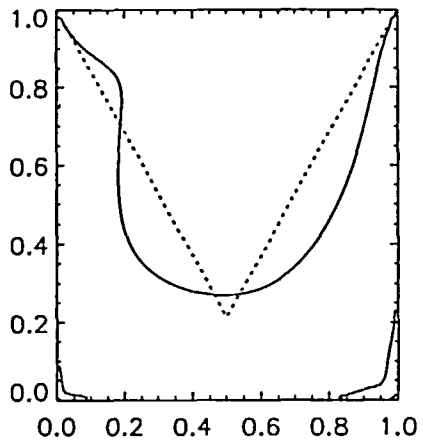

Figure 13 Null level of the computed solution ω^h with Re = 5, 64·64 control volumina

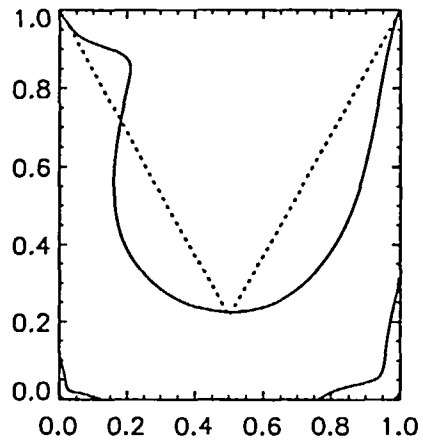

Figure 14 Null level of the computed solution ω^h with Re = 10, 128·128 control volumina

We note that the asymptotic solution (13) is also valid in the viscous case. To show the correspondence with the numerical results, we computed a solution for a Reynolds number Re = 20 on a graded mesh with 128·128 control volumina. The computation was performed with the Navier–Stokes solver LEARN[7]. The smallest control volume was of size $h = 0.001$ and positioned at the corners of the cavity. *Table 8* shows some angles ϕ that the null level of the vorticity ω of the numerical solution encloses with the driven side I. This angle is a sensitive quantitative indicator that demonstrates the coincidence of the asymptotic solution with the numerical results in a region near the corner. Again, the angles are about the given angle

$\phi_0 = 57.52°$ of the developed asymptotic solution (13) in a small region around the left corner of size of $d \approx 0.02$. The fact that we computed only a solution with a very low Reynolds number is not a deficiency in principle, because we have to use finer grids with increasing *Re*. Then, the computed solution will show the same local properties in a small region around the corner like the solution above with $Re = 20$. But the region, where the asymptotic solution is valid decreases with *Re*. For example, with doubling *Re* we have to halve the meshsize in order to keep the Peclet number constant and, therefore, to get the necessary resolution for the numerical solution around the corner. In *Figure 13*, the null level of ω of the computed solution on an equidistant grid with $64 \cdot 64$ control volumina and $Re = 5$ is shown, and in *Figure 14*, the null level of ω of the solution on a grid with $128 \cdot 128$ control volumina and $Re = 10$. The line which encloses exactly the angle ϕ_0 with the driven side I indicates that again the two numerical solutions are well described by the analytical solution (13) in a small region around the corner (except for the pollution effects for the point on the boundary and next to the boundary). Therefore, we can conclude that the derived asymptotic solution (13) is valid as well in a small region around the corner of the driven cavity in the case of viscous fluid flows.

REFERENCES

1 Apostolescu, V. Numerische Behandlung der stationären Umströmung einer Ecke bei zähen inkompressiblen Fluiden, *Technische Universität München*, LRZ-Bericht Nr. 8601 (1985)
2 Bjorstad, P. Numerical solution of the biharmonic equation, *PhD Thesis*, Dept. of Computer Science, Stanford University (1980)
3 Blum, H. The influence of reentrant corners in the numerical approximation of viscous flow problems, *Notes on Numerical Fluid Mechanics*, **30**, 37–46 (1989)
4 Griebel, M. Zur Lösung von Finite-Differenzen- und Finite-Element-Gleichungen mittels der Hierarchischen-Transformations-Mehrgitter-Methode, *SFB-Bericht Nr. 342/4/90 A*, Technische Universität München (1990)
5 Hackbusch, W. *Multigrid Methods and Applications*, Springer Verlag, Berlin (1985)
6 Hackbusch, W. *Theorie und Numerik elliptischer Differentialgleichungen*, Teubner Studienbücher (1986)
7 INVENT Computing GmbH, *Program LEARN*, Handbuch: Einführung in die Strömungsmechanik I und II (1993)
8 Kondrat'ev, V. A. Asymptotic of solution of the Navier–Stokes equation near the angular point of the boundary, *Applied Math. and Mech.*, **31**, 125–129 (1967)
9 Linden, J. Mehrgitterverfahren für das erste Randwertproblem der biharmonischen Gleichung und Anwendung auf ein inkompressibles Strömungsproblem, *GMD-Bericht Nr. 164*, Oldenbourg Verlag, München (1986)
10 Zink, L. Numerische Behandlung von Ecksingularitäten der biharmonischen Gleichung, Technische Universität München, *TUM-M8315* (1983)